

Original Research

Spatial-Temporal Evolution Pattern and Prediction Analysis of Rainfall Erosivity (1950-2020) in the Tibetan Plateau

Huihui Zhao¹, Yang Zhang², Bing Guo^{1,3}, Xiaodong Shao^{1,4},
Liping Li¹, Yangming Jiang^{1*}

¹Aerospace Information Research Institute, Chinese Academy of Sciences, Beijing 100101, China

²North China Power Engineering Co., Ltd. of China Power Engineering Consulting Group, Beijing 100120, China

³Shandong University of Technology, Zibo 255000, China

⁴Yunnan Tobacco Company Honghe Company, Mile, Yunnan 652300, China

Received: 16 December 2022

Accepted: 11 April 2023

Abstract

Analysing the temporal and spatial changes in regional rainfall erosivity can reveal the formation mechanism and succession process of water and soil loss. This is particularly relevant for ecologically fragile areas, such as the Tibetan Plateau. In this study, a gravity centre model, Hovmoller diagram, wavelet analysis, Mann-Kendall test, Rescale range analysis, and Daniel's trend test were used to analyse the spatial and temporal evolution pattern of rainfall erosivity on the Tibetan Plateau. The study used 0.25° spatial resolution data based on ERA5 correction from 1950-2020, which improved the spatial resolution and extended the time range of rainfall erosivity research on the Tibetan Plateau. The rainfall erosion in the southeast of the Tibetan Plateau was found to be severe and gradually decreased from the southeast to northwest. The average gravity centre of rainfall erosivity migrated from the southeast to the northwest. Regarding the time cycle, the average rainfall erosivity of the Tibetan Plateau changed rapidly each year, with an approximately 11-year cycle. Furthermore, the rainfall erosivity in the Tibetan Plateau showed a weak downward trend, which could continue to decrease in the future. Collectively, these results support regional ecological security and can help prepare prevention and control measures.

Keywords: rainfall erosivity, Tibetan Plateau, evolution pattern

Introduction

The Tibetan Plateau is the highest plateau in the world, with an average altitude above 4,000 m. The region has proven to be sensitive to climate

change and is ecologically fragile [1]. Since the mid-1950s, the Tibetan Plateau has experienced more significant warming than other regions at the same latitude [2]. Increased snowmelt and more frequent heavy precipitation events could lead to more severe soil erosion on the Tibetan Plateau. Understanding the rainfall erodibility of the Tibetan Plateau is important for its soil sustainability and water and food security [3].

*e-mail: jiangym_rs@126.com

Accurate calculation of rainfall erosion forces is essential for quantitative analysis and forecasting of regional soil erosion. Indeed, erosion force can be used to characterise and quantify the mechanisms and intensity of precipitation on soil erosion [4]. Rainfall erosivity is the potential capacity of rainfall to directly cause soil erosion and is an important indicator of the carrying capacity of regional resources and the environment. When the infiltration capacity is saturated, surface runoff causes soil erosion. Rainfall erosivity is one of the most important factors in soil erosion control; its spatial and temporal distribution plays a role in determining the patterns of soil erosion [5, 6]. Therefore, it is necessary to accurately estimate rainfall erosivity on a long-term scale and have a clear grasp of its spatial distribution and evolution to estimate regional soil erosion.

Researchers have used myriad data and methods to study rainfall erosivity in different regions of the world. For instance, Panagos used a set of regression models that combined the European scale rainfall erosivity database (REDES) [7] and the UERRA dataset [8] to reconstruct the annual rainfall erosivity for all of Europe and observe its spatiotemporal trend during 1961-2018 [9]. Meanwhile, high-resolution satellite precipitation products are often used to map continental scale rainfall erosion degree across the United States [10]. Additionally, three datasets (EMO-5 [6 h], E-OBS [24 h], and UERRA MESCAN-SURFEX [24 h]) have been directly evaluated via a grid-to-point analysis based on their ability to simulate station-specific event rainfall erosivity time-series. EMO-5 showed potential for simulating rainfall erosion events, the grid dataset for which performed better in Northern Europe than Southern Europe [11]. Moreover, three sets of gridded precipitation data were used to calculate the rainfall erosivity distribution in India [12], demonstrating the effectiveness of grid datasets in simulating rainfall erosion. In particular, Bangladesh utilised the Tropical Rainfall Measuring Mission 3B42 time-series product between 1998 and 2016 to investigate precipitation aggressiveness, concentration, and seasonality over various hydrological regions [13]. Meanwhile, more than 100 studies have been performed on rainfall erosion in Brazil, of which ~42% have been applied to construct erosion maps. The most commonly used interpolation techniques include the Kriging method, artificial neural network (ANN), and inverse distance weighting method (IDW) [13].

Most studies using rainfall gauge data use spatial interpolation methods to predict and map the rainfall erosivity of the transition region [10]. Methods include inverse distance weighting, radial basis function, regression, and several Kriging methods [7, 14-18]. These methods calculate the rainfall erosivity of a single point using the measured rainfall data of meteorological stations. Subsequently, the rainfall erosivity spatial distribution is obtained by extrapolating the rainfall erosivity of a single point to a wider area using the

spatial interpolation method. However, interpolated rainfall erosion rate values often have considerable uncertainty [7, 14, 15].

According to Panagos et al., sites with high-frequency data on rainfall estimation have relatively low average erosion rates [19]. In areas where data availability is scarce, remote measurement of precipitation data can help estimate rainfall erosivity [20, 21]. Currently, due to a lack of data, most rainfall erosion is based on long-term estimations, beyond 10 years in certain regions. This limits the further analysis of rapid erosion in most parts of the world [19, 22, 23]. Compared with *in situ* observations, gridded precipitation data (e.g., based on satellite, reanalysis, and fusion datasets) are not limited by terrain and can provide continuous precipitation data [24]. These data have been widely used to estimate rainfall erosivity, especially *in situ* area observations [3] in Germany [25], the United States [26] and other regions [27].

To date, many rainfall erosivity studies on the Tibetan Plateau have used empirical methods [28-36], revealing that weather station scarcity can significantly reduce the accuracy of rainfall erodibility estimations in areas with complex topography and climate on the Tibetan Plateau [34]. Indeed, the accuracy of estimating rainfall erodibility on the Tibetan Plateau is low due to the scarcity of current empirical estimation models and historical weather stations [27]. The accuracy of rainfall erosivity estimates depends primarily on the spatial and temporal accuracy of precipitation data, particularly in areas such as the Tibetan Plateau, where seasonal and regional precipitation patterns exhibit significant variability due to westerly winds, Indian monsoons, and land-atmosphere interactions [19, 27].

Limited data resolution and time length data have prevented the analysis of long-term spatio-temporal precipitation erosivity and variation patterns for different time scales on the Tibetan Plateau. In particular, few studies have reported on the temporal and spatial evolution of rainfall erosivity in the Tibetan Plateau based on extended time series and high-resolution data using sufficiently comprehensive analytical methods. Accordingly, the current study applies various spatiotemporal analysis methods and long-time series data to analyse the evolution law and changes in the erosivity of the Tibetan Plateau from the time and space dimensions. The primary aim of this study is to characterize changes in the patterns of rainfall erosivity on the Tibetan Plateau along different time scales and to provide information for future ecological environment protection of the Tibetan Plateau.

Experimental

Data Source

The study area is the Tibetan Plateau (26-40°N, 73-105°E) located in southwestern China and covering

an area of approximately 2.5 million km². The elevation range of the Tibetan Plateau is 84-8246 m (average: 4379 m). Precipitation in the south-eastern Tibetan Plateau is influenced by the warm and humid Indian monsoon, while in the western Tibetan Plateau, it is influenced by the mid-latitude westerlies [1]. Annual precipitation is most intense between May and October [29], and shows a spatial pattern of wet east to west with dry in the centre [27].

A scarcity of weather stations can significantly reduce the accuracy of rainfall erosivity estimates in areas with complex topography and climate, such as the Tibetan Plateau [28, 29]. Consequently, accurate rainfall erosion rate estimations on the Tibetan Plateau are low due to the scarcity of historical weather stations and current empirical estimation models. Precipitation data with high spatial and temporal resolution are needed to calculate rainfall erosion rates on the Tibetan Plateau.

Compared with other gridded precipitation datasets, ERA5 successfully reproduces interannual and interdecadal variability of precipitation, reflecting spatial and temporal patterns [37]. ERA5 is marginally better at detecting long-term daily precipitation across the Tibetan Plateau [38], although deviations in precipitation are also reported [39].

An annual rainfall erosivity dataset with high resolution for the Tibetan Plateau from 1950-2020 was used. It included station-based precipitation data from a dense network of weather stations and reanalysis data. This dataset was generated from 1-min field rainfall data from 1787 meteorological stations and long-term ERA5 rainfall data with a spatial resolution of 0.25°. The dataset provided a unique view of small to large-scale features in rainfall erosivity variability over the Tibetan Plateau, where it is not easy to obtain long-term *in situ* precipitation data with sufficient spatiotemporal resolution [27].

Methods

The gravity centre model, Hovmoller diagram, wavelet analysis, and Mann Kendall test were used in this study. The gravity centre model and Hovmoller diagram can explain the overall movement direction and trend of soil erosion. The M-K analysis is widely used for trend analysis of time series [40, 41]. The advantage of the M-K test is that the series does not need to conform to a certain sampling distribution, thereby avoiding the potential influence of outliers [42, 43]. For rainfall erosivity of the Tibetan Plateau, the M-K test was used to detect trends and abrupt changes. The CWT is widely used to detect the periodicity of time series [42, 44]. Among many wavelet functions, the Morlet wavelet function provides a good balance between time and frequency localizations and is, thus, most suitable for studying temporal variation in rainfall erosivity [45].

Hovmoller Diagrams

The Hovmoller diagram is commonly used in weather and climate diagnostics to analyse coherent signals and was used in the current study to analyse the cumulative longitude or latitude of rainfall erosivity [46].

A Hovmoller diagram is a two-dimensional plot that presents the time–latitude variations of a longitudinally averaged variable [47]. In 1949, Ernest Hovmoller created a diagram capable of showing movement in static pictures. A cross between a map and a graph, the figure is known today as a Hovmoller Diagram. It is a two-dimensional plot showing how the value of some quantity varies in space and time; one axis refers to time and the other to spatial location, which is typically longitude or latitude in meteorological studies.

The Hovmoller diagram is commonly used in weather and climate diagnostics to analyse coherent signals and was used here to analyse the cumulative value of rainfall erosivity in longitude or latitude [46].

Gravity Centre Model

A gravity centre model was derived from the field of physics and refers to the point at which the gravity force is exerted equally on each part of an object [48]. The centre of gravity is a helpful estimator for assessing certain redistribution trends and is represented as a point that shows the average location of a weighted object. In an early study, Hilgard used it for detecting trend changes in the population distribution of the United States [49]. Over the years, extensive research regarding centres of gravity have focused on population [50, 51], economics [52], urbanisation [53], land utilisation [54], and environmental pollution [55]. In the field of rainfall erosivity, the spatial variation characteristics of the gravity centre can reflect the degree of change in the rainfall erosivity level. In this study, the rainfall erosivity level of grid i is z_i , and the average value of a region that is composed of space units (grids) is defined as \bar{x} and \bar{y} in Cartesian coordinates, which can be expressed as follows:

$$\bar{x} = \left(\sum_{i=1}^{i=n} z_i x_i \right) / \left(\sum_{i=1}^{i=n} z_i \right)$$

$$\bar{y} = \left(\sum_{i=1}^{i=n} z_i y_i \right) / \left(\sum_{i=1}^{i=n} z_i \right)$$

Rescale Range Analysis

A dimensionless ratio, R/S, in a rescaled range analysis (R/S analysis), was utilised to calculate the rescale range of each subsequence [56, 57]. The Hurst index (H) of the R/S analysis is an indicator used to measure the correlation and trend intensity of a time

series. Its value range is $0 < H \leq 1$. Whether or not the time series is completely random, a trend component of persistence or anti-persistence was determined depending on the size of the H . Different values corresponded to the following situations. (1) $H = 0.5$: the sequence is a random process, and the trend does not affect the future. (2) $0 < H < 0.5$: the time series presents anti-persistence, that is, the future trend is opposite to the past. The closer the H value is to 0, the stronger the anti-persistence. (3) $0.5 < H < 1$: the time series is continuous, meaning that the future trend is the same as the past trend. The larger the H value, the more evident the trend.

Mann-Kendall Test

Traditional classical statistical methods analyse and predict static data in a time series, however, many time series data do not conform to this hypothesis. Therefore, we used the Mann-Kendall test, a non-stationary time series analysis method [40, 41] as it does not require the sample to follow a specific distribution and is not disturbed by a few outliers [42, 43]. When the standardised test statistic is positive, there is an upward tendency. When the standardised test statistic is negative, a downward tendency is observed [58, 59].

Mutation detection and cycle tests are important methods for analysing change and development in a long time series. You can clearly and intuitively understand the development process through mutation detection and cycle change. The Mann-Kendall test can also be used to test the mutation point of a sequence. When UF_k (positive sequence statistics) and UB_k (inverse sequence statistics) intersect, and the intersection point is within the critical line, the time corresponding to the intersection point is the time when the mutation begins. Meanwhile, when $UF_k > 0$, the sequence shows an upward trend. When $UF_k < 0$, the sequence exhibits a downward trend. If UF_k exceeds the critical value, an evident change in trend occurs [60].

Daniel's Trend Test

The Daniel Trend Test method was used to analyse temporal variation trends [61]. Daniel's trend test is a statistical analysis method based on the Spearman's rank correlation coefficient [62]. This method belongs to a class of non-parametric tests and adopts Spearman rank correlation coefficient to assess the significance of changes in trend. In the Spearman rank correlation test, the accuracy of time series data need not be considered. However, the time series data must be transformed into rank sequentially. The quantity of data points must, typically exceed four. To achieve Y_1, Y_2, \dots, Y_N , by sorting the time series data according to the data value from small to large, the corresponding serial numbers are X_1, X_2, \dots, X_N . The rank correlation coefficient used in statistical tests was as follows:

$$r_s = 1 - \frac{6 \sum_{i=1}^N d_i^2}{N^3 - N}$$

where $d_i = X_i - Y_i$, N is the amount of data; $r_s > 0$ represents an upward trend, and vice versa [63].

Wavelet Analysis (Morlet)

Wavelet analysis is a powerful tool well-suited to study multiscale, nonstationary processes occurring over finite spatial and temporal domains. Recently, wavelet transform has found numerous applications in Geophysics [44, 64]. Wavelet transformations were used to analyse the multi-frequency characteristics of the non-stationary time series. In addition, since the Morlet continuous complex wavelet transformation can provide both phase and amplitude information of time series variations, the Morlet wavelet function is commonly used in the study of climate-related sequences:

$$\varphi_0(\mu) = \pi^{-1/4} e^{i\omega_0\mu} e^{-\mu^2/2}$$

where ω_0 refers to the frequency, which is dimensionless.

Results and Discussion

Analysis of Spatial Distribution Characteristics

Fig. 1 shows that the rainfall erosivity in the southeast of the study area was the highest and caused the most serious soil erosion. Overall, there was a gradual decreasing trend from southeast to northwest, which is consistent with the spatial distribution of precipitation on the Tibetan Plateau and has a high correlation with elevation and topography. The region with the highest elevation in the south had the highest precipitation erosion force, indicating that the soil erosion by precipitation was the most serious in the south-eastern region.

The north-western area showed a relatively uniform spatial distribution, with strong erosion in local areas, such as near (82°E, 31°N) and (88°E, 29°N). Key regions with large rainfall erosivity potential are concentrated in the Bomi-West Sichuan and Dawang-Chayu areas. The largest area-averaged annual rainfall erosivity in the Tibetan Plateau reached 15,997 MJ·mm·ha⁻¹·h⁻¹·yr⁻¹.

The study area maintained a high rainfall erosion index in the southern region from the 1950s to the 1990s, with minimal fluctuation over 50 years, indicating that rainfall erosion has been severe in this part of the region, while all other regions had a low rainfall erosivity index (Fig. 2). These five periods showed large extremes, with a maximum value of 17,331.3 MJ·mm·ha⁻¹·h⁻¹·yr⁻¹ in the 1990s, which represented the maximum of the seven periods, indicating that a certain region was continuously subjected to high-intensity rainfall erosion. Moreover, the overall spatial distribution of the

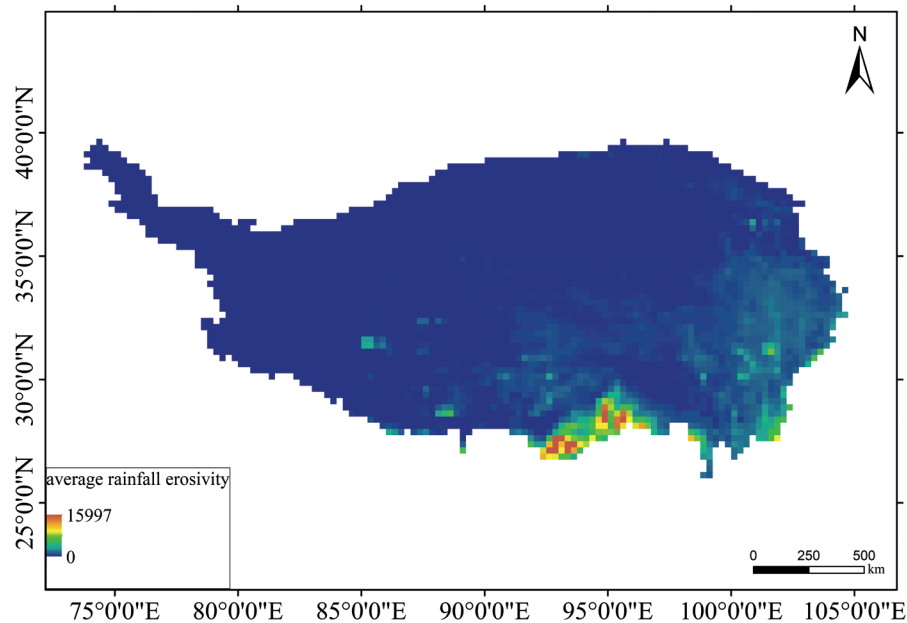


Fig. 1. Average rainfall erosivity map of the Tibetan Plateau from 1950-2020.

period from the 1950s to the 1990s was more uneven. As shown in Fig. 2, more regions have increased their brightness since 2000, but this does not mean that the rainfall erosion index has increased. This is due to a rendering effect caused by the smaller maximum values in these two periods.

Gravity Centre Analysis

The gravity centre of rainfall erosivity on the Tibetan Plateau over 71 years shifted within 200 km (Fig. 3). The average centre of gravity of the rainfall erosion force for the entire 71-year period was applied as the coordinate origin. This was used to analyse the spatial distribution characteristics of the centre of gravity of the rainfall erosion force for each year. The number of gravity centres of rainfall erosion force located in different quadrants of the coordinate system were counted and calculated (Fig. 4a); the number in the southeast and southwest quadrants were the largest, accounting for 32.4% and 23.9%, respectively, indicating that the soil erosion by rainfall was more serious in these regions of the study area. Meanwhile, the proportion of rainfall erosion force gravity centres in the northeast and northwest quadrants was lower at 21.1% and 22.5%, respectively.

As China is significantly influenced by the monsoon, the coordinate system of Fig. 4a was rotated 45° counter-clockwise to obtain a new coordinate system, and the number and proportion of rainfall erosion force gravity centres in each quadrant were counted and calculated. The east quadrant had the largest weight of the gravity centre of rainfall erosion force, 29.6%, followed by the south quadrant (26.8%) and the west quadrant (23.9%), with the north quadrant having the smallest weight

(19.7%; Fig. 4b). The study area can also be divided into two parts according to the coordinate axes; the gravitational weight of the rainfall erosion force in the southeast quadrant was 58% greater than that in the northwest quadrant (42%), indicating that rainfall erodes the soil more severely in the southeast region than in the northwest.

To further explore the spatial variability characteristics of the gravity centre of rainfall erosion force, the rainfall erosion force was analysed on a 10-year scale throughout the study cycle, and the migration direction of the gravity centre was determined (Fig. 5). From the 1950s to the 1970s, the rainfall erosion force gravity centre moved in variable directions, first to the southwest, then to the west and to the east. The rainfall erosion force centre of gravity shifted noticeably to the northwest after 1980, indicating that rainfall erosion was severe in the northwest of the study area over the following period.

Hovmoller Diagram

The Hovmoller diagram was used in this study to analyse the time-longitude or time-latitude features of hourly rainfall propagation. To create the Hovmoller diagrams, rainfall erosivity was averaged over the longitudinal or latitudinal planes from 1950 to 2020.

From the Hovmoller diagram of longitude accumulation (Fig. 6a), it was observed that the average rainfall erosivity of the Tibetan Plateau was unevenly distributed. In particular, 92°E, 96°E, and 100°E-104°E had the highest average rainfall erosivity, with centrelines located at 94°E, 95°E, and 102°E. The average rainfall erosivity within the range of less than 65°E, 65°E-78°E, and 104°E-108°E was the lowest,

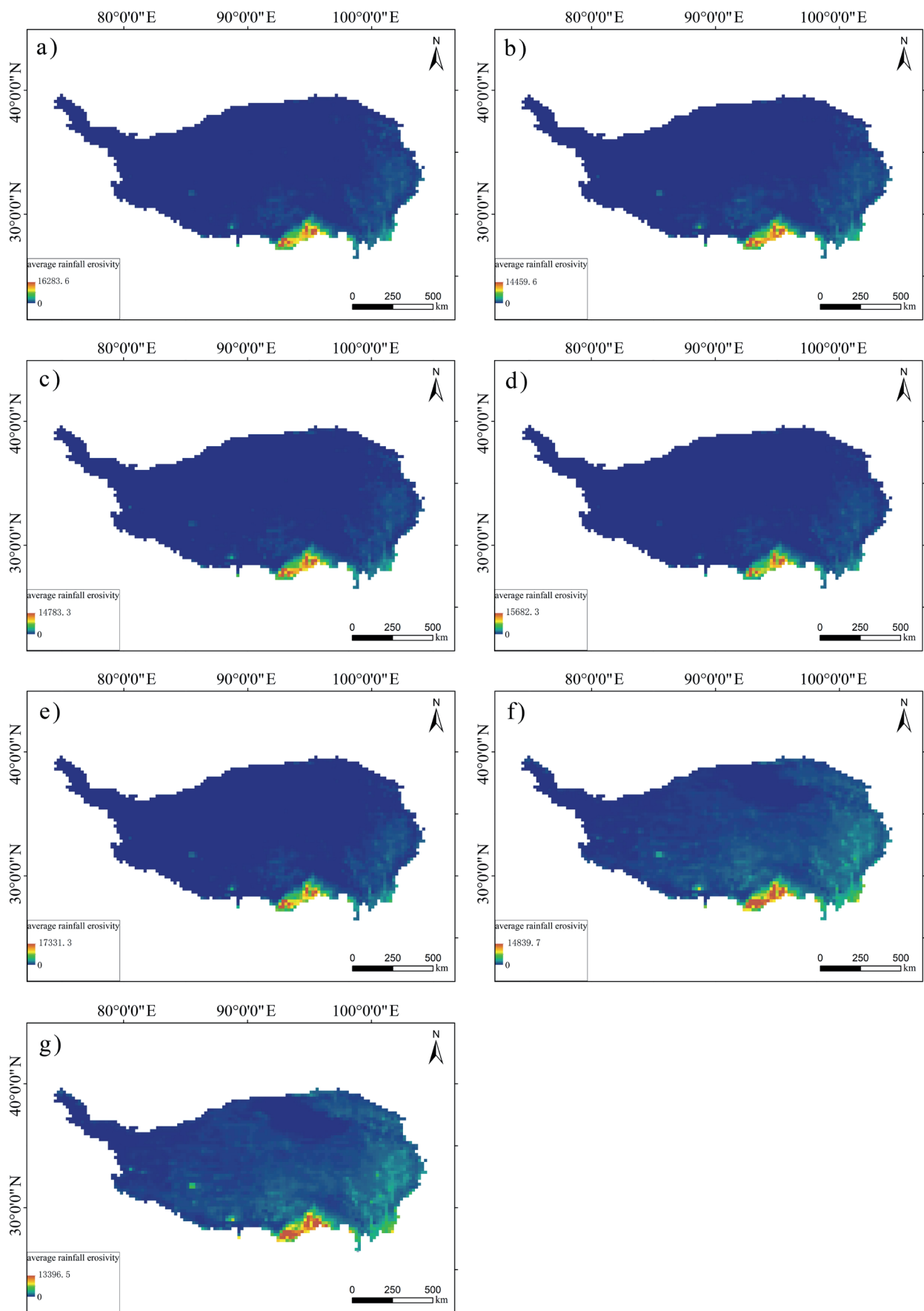


Fig. 2. 10-year average rainfall erosivity distribution map of the Tibetan Plateau for 1950-2020. a) 1950s, b) 1960s, c) 1970s, d) 1980s, e) 1990s, f) 2000s, g) 2010s.

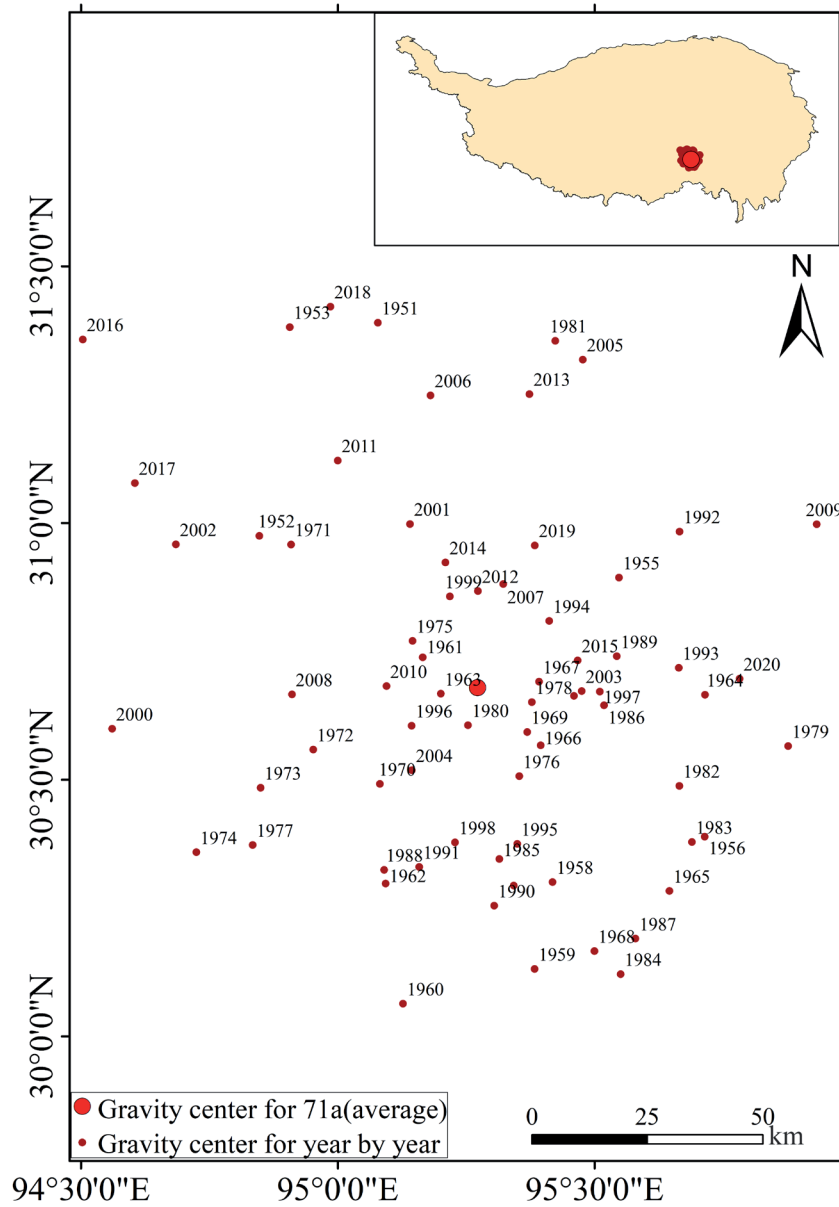


Fig. 3. Spatial distribution of annual rainfall erosivity gravity centres from 1950 to 2020.

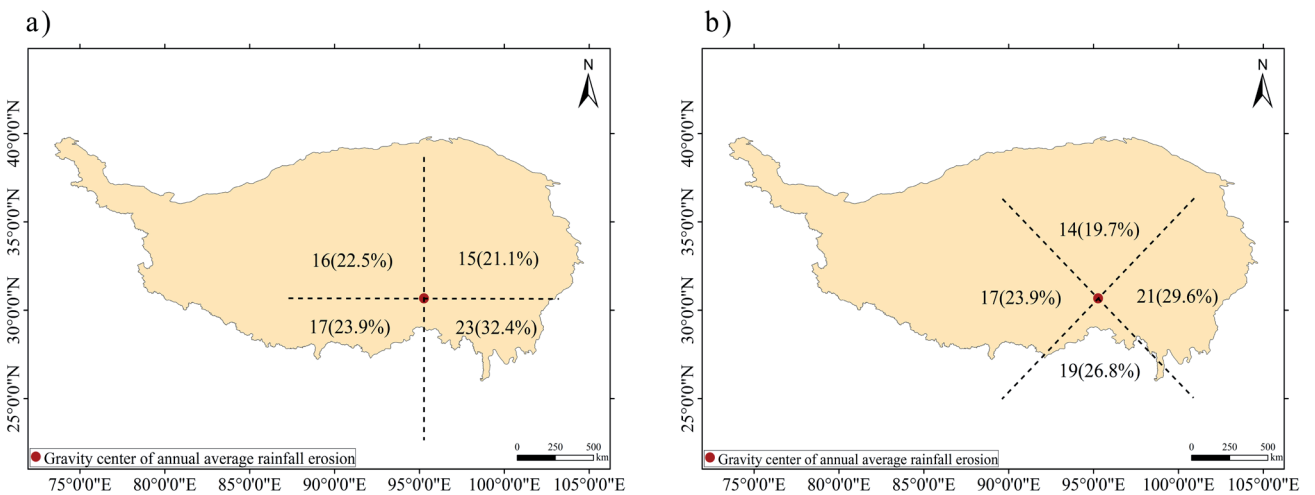


Fig. 4. Distribution proportion of annual average rainfall erosion gravity centres during 1950–2020: a) ortho axis, b) oblique axis.

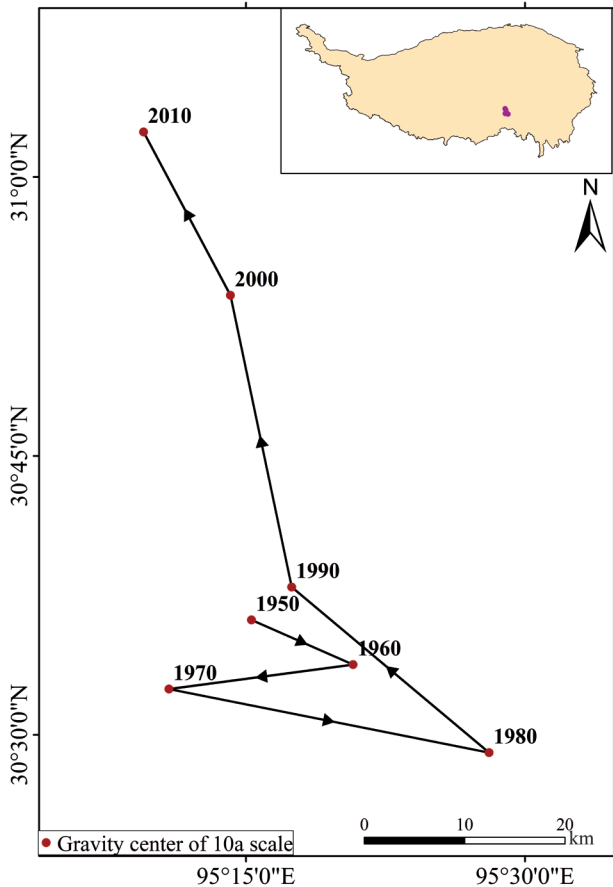


Fig. 5. Migration trajectory of the rainfall erosion gravity centres on a 10-year scale.

and the average rainfall erosivity in other regions was in the medium range.

From the perspective of the cumulative Hovmoller diagram of latitude (Fig. 6b), the average rainfall erosivity of the Tibetan Plateau also showed uneven distribution. That is, 27°N-29°N had the highest average rainfall erosivity, showing a gradual decreasing trend from the regional centreline of 28.5°N to the north.

The Hovmoller diagrams also reflect the time cycle characteristics of the average rainfall erosivity of the Tibetan Plateau. The rainfall erosivity changed rapidly over time, particularly in areas with high average rainfall erosivity. From 1985 to 2020, a noticeable periodicity of 27°N-29°N was observed in the 92°E-96°E range of the longitude cumulative Hovmoller and 96°E of the latitude cumulative Hovmoller. The highest points of the cycle occurred during 2020a, 2009a, 1998a, and 1987, suggesting that the cycle was approximately 11 years. In the range of longitude 85°E-92°E, periodicity was also observed, with the cycle peaks at 1976a, 1965a, and 1954a, also showing a cycle of approximately 11 years.

Periodic Characteristic Analysis

The periodic variation of rainfall erosivity in the Tibetan Plateau was analysed by the wavelet method (Fig. 7). The power spectrum analysis results of rainfall erosivity in Fig. 7 further revealed the periodic variation characteristics of rainfall erosivity, and the solid black line represents the significant 0.05 test marker line.

From the wavelet power spectrum after excluding the influence of the boundary, it was observed that the high energy areas were concentrated between 26-45a

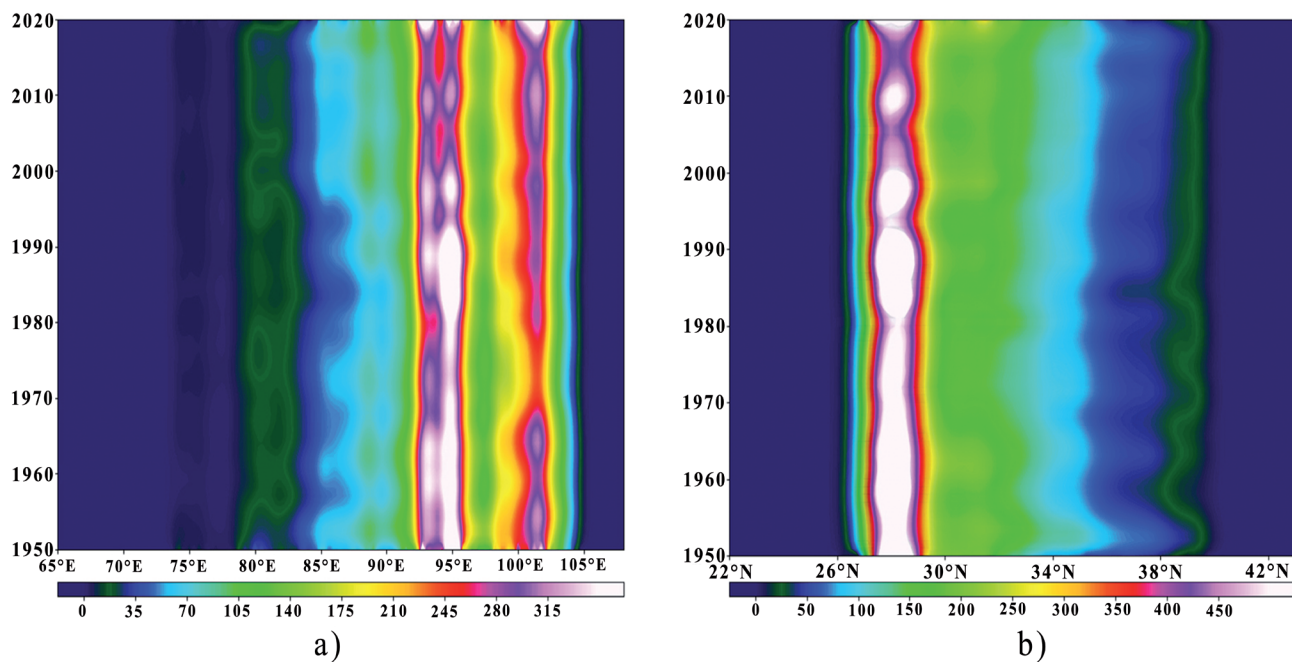


Fig. 6. Hovmoller diagram of average rainfall erosivity of the Tibetan Plateau. a) Hovmoller diagram of longitude accumulation, b) Hovmoller diagram of latitude accumulation.

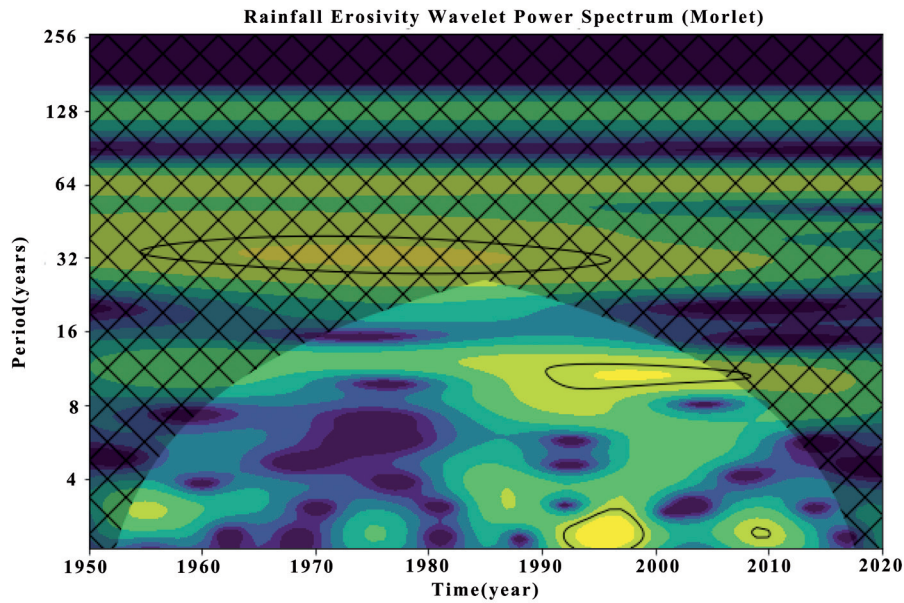


Fig. 7. Wavelet power spectrum of rainfall erosivity for the Tibetan Plateau from 1950 to 2020.

in the 1955-1998 range, 9-13a in the 1992-1998 range, and 2-3a in the 1993-1999 range, where the wavelet power reached a significant level on the 9-13a scale. It also reached a significant level on the 2-3a scale with a noticeable cycle. There was no evident periodic change in other years, which also confirms the above characteristics that rainfall erosivity fluctuates greatly, but overall change trends are not evident.

Mann-Kendall Test

The results of the Mann-Kendall mutation test for rainfall erosivity over the 71-year study period are shown in Fig. 8. When $UF > 0$, the time series exhibited an upward trend, and when $UF < 0$, it showed a

downward trend. If the rising or falling trend exceeded the 0.05 significance test boundary line, a significant change trend occurred. When the two time series UF and UB intersected and were within the boundary line of the significance test, the intersection represented a sudden change point, and its corresponding time node was the time when the statistical series had a sudden change.

With the exception of 1950-1955 and 1964, UF statistics in other years were < 0 . Hence, rainfall erosivity was generally declining, and UF statistics during the 1970-1990 period exhibited a significance level $> U_{0.05}$. A downward trend was noticeable from 1970 to 1990 and was maintained after 1997, however, was less evident. UF statistics and UB statistics intersected

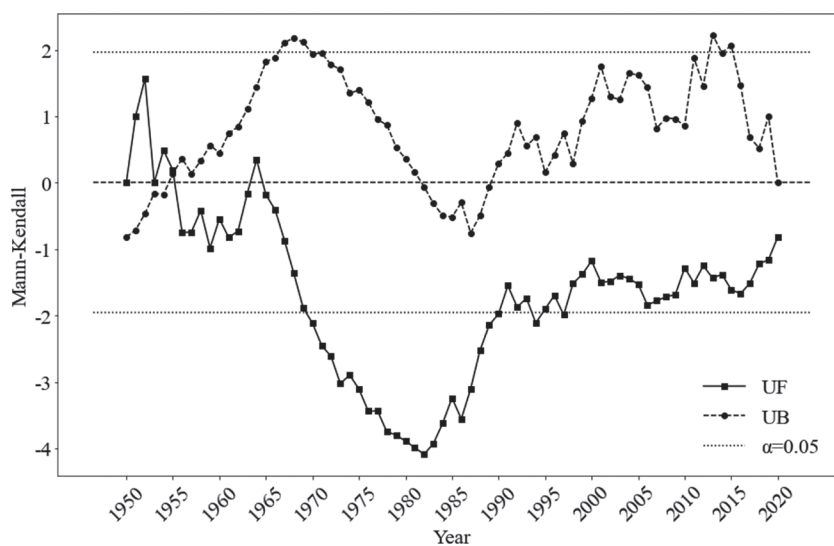


Fig. 8. Mann-Kendall test of rainfall erosivity for the Tibetan Plateau.

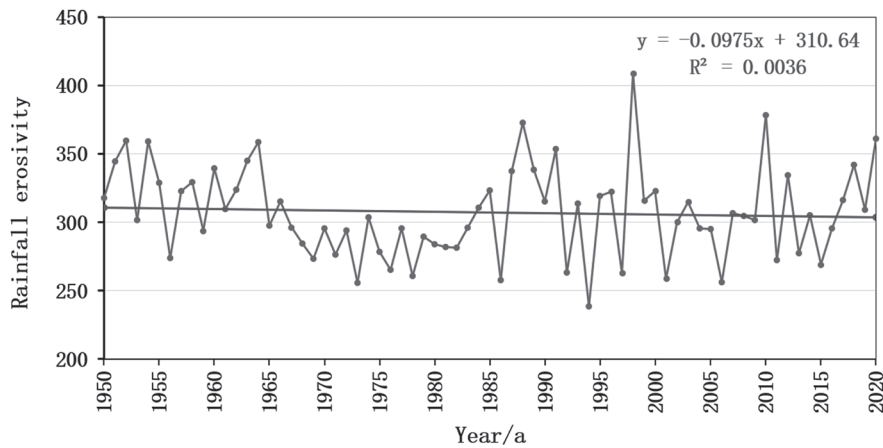


Fig. 9. Mean annual rainfall erosivity for the Tibetan Plateau from 1950-2020.

in 1954, and the absolute value of the intersection was <1.96, lower than the $U_{0.05}$ significance level. As such, no significant mutation point nor mutation interval in rainfall erosivity data occurred in the Tibetan Plateau over the 71 years.

Trend Prediction

Overall Trend Analysis

The trend coefficient of the annual average rainfall erosivity of the Tibetan Plateau in the past 71 years was -0.0975 , indicating that it is decreasing (Fig. 9). The Hurst index was 0.6169 , indicating that the study area will continue to show a weak downward trend in the future. The statistical value of Z was -0.7972 , and the Daniel coefficient was -0.0847 , both of which did not reach a significant level. Hence, it cannot be concluded that the trend will decline in the future.

Analysis of 10-year Scale Trend

Through linear trend estimation, M-K test, and R/S analysis, the intensity of rainfall erosivity at 10-year intervals was assessed. The time periods were 1950-1959, 1960-1969, 1970-1979, 1980-1989,

1990-1999, 2000-2009, and 2010-2019 (Table 1). The results of the linear trend analysis and Daniel Index identify four periods of decline and three periods of increase. Z statistics did not reach a significant level, indicating that the downward trend was not evident. In these seven periods, the Hurst index of only two periods was <0.5 , indicating that the change trend of rainfall erosivity was not random and had inherent persistence over the 10-year scale. Based on the above analysis and the trend prediction of rainfall erosivity on a 10-year scale, it can be concluded that the rainfall erosivity of the Tibetan Plateau will likely continue to exhibit a downward trend in the future.

Discussion

Considering the effects of soil erosion by rainfall on the entire environment, it is expected that the rainfall erosivity map generated in this study can be used to estimate amounts of soil loss and identify regions vulnerable to soil erosion. Moreover, it provides theoretical references for the prevention and control of soil erosion, as well as the formation and evolution mechanisms of ecological security patterns in the Tibetan Plateau [65].

Table 1. Statistical analysis of rainfall erosivity prediction at 10-year scale for the Tibetan Plateau.

Period (year)	Trend statistics	Z statistic	Hurst Index	Daniel Index
1950-1959	-3.7559	-1.1472	0.5513	-0.3575
1960-1969	-6.4334	-0.8069	0.6579	-0.7212
1970-1979	-0.9149	1.0014	0.2539	-0.2121
1980-1989	7.9121	0.0680	0.6184	0.6848
1990-1999	2.9881	-0.1166	0.5462	0.1757
2000-2009	-0.0643	0.1458	0.3849	-0.0666
2010-2019	-1.2733	0.0486	0.5484	0.0424

The dataset used in this study, based on the ERA5 corrected and calculated precipitation erosivity dataset, provides a unique view of large-scale to local-scale features in rainfall erosivity variability over the Tibetan Plateau, where it is relatively impossible to obtain long-term *in situ* precipitation data with sufficient spatiotemporal resolution. By absorbing a large number of ground observations, atmospheric detection data, and remote sensing data, ERA5 provides a reasonable spatial and temporal variation of large-scale precipitation [27]. It is also worth noting that certain uncertainties are inevitably associated with newly reconstructed datasets. Nevertheless, the fusion of precipitation data from different sources tends to be useful for the estimation of rainfall erosivity, particularly in regions with limited ground data. However, one can expect that technological development over the next decades will lead to improved accuracy of satellite-based and grid data products, which can serve as input for the dynamic rainfall erosion models.

In this study, the gravity centre model, Hovmoller diagram, wavelet analysis, Mann-Kendall test, and other methods were introduced to analyse the rainfall erosivity of the Tibetan Plateau in time and space. Spatial distribution is characterized by a decreasing trend from the southeast to the northwest, which is in accord with previous studies [5, 29, 66, 67]. The gravity centre model and Hovmoller diagram measure the overall distribution of a certain attribute in the region, and their distribution trend can reveal uneven degrees of the attribute in the spatial distribution [68]. Although the gravity centre model has been widely applied in the field of social and economic research [69, 70], its application in the discipline of rainfall erosivity has been less reported. Introducing the gravity centre method to the study of changes in rainfall erosivity trends is conducive to revealing the spatial change characteristics of rainfall erosivity on the Tibetan Plateau [71].

On the Hovmoller diagram, the annual rainfall erosivity 85°E is relatively high, primarily because the north-south pattern of the Hengduan Mountains and valleys in eastern Tibet is conducive to the entry of water vapor from the Indian Ocean, making rainfall in this area relatively abundant. In contrast, there is relatively little precipitation in northwest Tibet, due to the obstruction of the Himalayas system, coupled with high altitude and low temperature; the corresponding rainfall erosivity is low, which is relatively consistent with the north of 35°N and west of 85°E values on the Hovmoller diagram. However, in the Yarlung Zangbo River basin, due to the low terrain, sufficient water and heat, and high rainfall erosivity, the gravity centre shifts around the large bend of the Yarlung Zangbo River. Additionally, precipitation in the rainy season has a pronounced vertical differentiation in the plateau; with the increase in altitude, precipitation significantly decreases and then increases [69, 70], leading to complexity in the spatial distribution of rainfall

erosivity, which also presents complex texture in the Hovmoller diagram.

Given that most of the Earth's energy originates from the sun, changes in solar energy affect the climate and rainfall patterns. According to relevant studies, wavelet analysis of annual rainfall data and sunspot number shows a wavelet cross-power of approximately 11 years for both time series [72]. Thomas et al. reported that the periodicity of sunspot numbers and rainfall estimated by Fourier analysis is in agreement with wavelet analysis. The cross-wavelet transform also indicates a distinct 8-12-year correlation between sunspot number and rainfall [73]. In the current study, the rainfall erosivity presents a period of approximately 11 years, indicating that the characteristics of rainfall erosion change in response to the solar magnetic cycle, and a specific relationship exists between solar activities and rainfall erosion.

In terms of the characteristics of the trends over years, the annual rainfall erosion degree fluctuated greatly, however, did not exhibit an evident increasing or decreasing trend over the past 71 years. However, based on trend analysis, a weak downward trend will be observed in the future, which agrees with the results of previous studies [2, 13, 29, 74]. Although the length of the precipitation data series used in different studies differs, the soil erosivity of the Tibetan Plateau is one of the few regions in the world with a downward trend. In terms of spatial distribution, the R factor generally exhibits a decreasing trend from the southeast to the northwest, which is consistent with previous research results [29, 67, 74]. This is accounted for by the study area being affected by westerly circulation, the North Atlantic Oscillation, topography, and geographical factors, forming a unique pattern of precipitation and erosivity in the Tibetan Plateau [67, 75]. This is similar to the spatial distribution characteristics of rainfall erosivity throughout China [76], as well as within the Songhua River basin [77], Loess Plateau region [78, 79], and southwest region [80]. In particular, the blocking effect of mountains on moist airflow causes the rainfall on the windward slope and the intensity of rainfall erosivity to increase. Meanwhile, the increase in altitude will also have an amplification effect on rainfall erosivity [45, 77, 80, 81].

Although the data applied in the current study is superior to that of other related studies in terms of spatial resolution and time range, the accuracy and resolution of precipitation erosivity can be further improved by combining higher precision terrain data and meteorological data. Regarding trend prediction, given the insufficient time range of historical data, the long-term trend evolution law and short-term prediction accuracy of precipitation erosivity in the Tibetan Plateau may not be sufficiently accurate. Hence, future research should incorporate the artificial intelligence spatial-temporal prediction method to obtain more accurate prediction results based on a small number of samples.

Conclusions

Based on the ERA5 corrected and calculated precipitation erosivity data set, which expanded the time range of the dataset in the Tibetan Plateau, this study analysed the spatial and temporal distribution pattern of rainfall erosivity throughout the Tibetan Plateau, evaluated the decades-scale interannual changes in rainfall erosivity, and carried out trend analysis. Accordingly, the following conclusions can be drawn:

First, the rainfall erosion in the southeast of Tibetan Plateau has been the most severe over the past seven decades. Although the rainfall erosion in the northwest of the study area is relatively less severe, the spatial distribution differentiation has declined over the past 20 years. Second, the gravity centre shifted from the southeast to the northwest, especially after 1980. Consequently, rainfall will likely erode the north-western portion of the study area in the future. Third, based on the time dimension, the average rainfall erosivity of the Tibetan Plateau changes rapidly within one year, however, follows an approximately 11-year cycle, especially in regions with high average rainfall erosivity. Finally, the rainfall erosivity in the Tibetan Plateau continues to fluctuate, showing a weak downward trend, which is expected to be maintained in the future.

This study has certain strengths in that it comprised various spatiotemporal analysis methods, combined with long time series and high-resolution precipitation erosivity data to analyse the evolution law and trend in the Tibetan Plateau Plateau erosivity from the dimensions of time and space. Moreover, the dataset provides a unique view of the large-scale to local-scale characteristics of the Tibetan Plateau rainfall erosivity patterns. Given the difficulty associated with obtaining long-term on-site precipitation data with sufficient spatial and temporal resolution, the evolution analysis with higher resolution and a longer time cycle is valuable. As such, the results of this study serve as an important reference for further analysis of the spatiotemporal evolution pattern of soil erosion, as well as the formation of, and evolution mechanism associated with the, ecological security pattern in the Tibetan Plateau. In particular, these findings can be applied to design protection policies for specific regions, which will help to predict the evolution of ecosystem structures and formulate appropriate countermeasures to adapt to climate change. Finally, considering that soil erosion is a key land degradation indicator within the framework of sustainable development goals (SDGs), the proposed results have important relevance for policy implementation.

Acknowledgments

This research was supported by the National Natural Science Foundation of China (52101405).

Conflict of Interest

The authors declare no conflict of interest.

References

1. YAO T.D., THOMPSON L., YANG W., YU W.S., GAO Y., GUO X.J., YANG X.X., DUAN K.Q., ZHAO H.B., XU B.Q., PU J.C., LU A.X., XIANG Y., KATTEL D.B., JOSWIAK D. Different glacier status with atmospheric circulations in Tibetan Plateau and surroundings. *Nature Climate Change*. **2** (9), 663, **2012**.
2. CHEN Y., DUAN X., ZHANG G., DING M., LU S. Rainfall erosivity estimation over the Tibetan plateau based on high spatial-temporal resolution rainfall records. *International Soil and Water Conservation Research*. **10** (3), 422, **2022**.
3. TENG H., LIANG Z., CHEN S., LIU Y., VISCARRA ROSSEL R.A., CHAPPELL A., YU W., SHI Z. Current and future assessments of soil erosion by water on the Tibetan Plateau based on RUSLE and CMIP5 climate models. *Science of the Total Environment*. **635**, 673, **2018**.
4. HAMLAOUI-MOULAI L., MESBAH M., SOUAG-GAMANE D., MEDJERAB A. Detecting hydroclimatic change using spatiotemporal analysis of rainfall time series in Western Algeria. *Natural Hazards*. **65** (3), 1293, **2013**.
5. PANAGOS P., BORRELLI P., MEUSBURGER K., YU B., KLIK A., JAE LIM K., YANG J.E., NI J., MIAO C., CHATTOPADHYAY N., SADEGHI S.H., HAZBAVI Z., ZABIHI M., LARIONOV G.A., KRASNOV S.F., GOROBETS A.V., LEVI Y., ERPUL G., BIRKEL C., HOYOS N., NAIPAL V., OLIVEIRA P.T.S., BONILLA C.A., MEDDI M., NEL W., AL DASHTI H., BONI M., DIODATO N., Van OOST K., NEARING M., BALLABIO C. Global rainfall erosivity assessment based on high-temporal resolution rainfall records. *Scientific Reports*. **7** (1), **2017**.
6. YUE T., XIE Y., YIN S., YU B., MIAO C., WANG W. Effect of time resolution of rainfall measurements on the erosivity factor in the USLE in China. *International Soil and Water Conservation Research*. **8** (4), 373, **2020**.
7. PANAGOS P., BALLABIO C., BORRELLI P., MEUSBURGER K., KLIK A., ROUSSEVA S., TADIĆ M.P., MICHAELIDES S., HRABALÍKOVÁ M., OLSEN P., AALTO J., LAKATOS M., RYMSZEWICZ A., DUMITRESCU A., BEGUERÍA S., ALEWELL C. Rainfall erosivity in Europe. *Science of the Total Environment*. **511**, 801, **2015**.
8. DAHLGREN P., LANDELIUS T., KÅLLBERG P., GOLLVIK S. A high-resolution regional reanalysis for Europe. Part 1: Three-dimensional reanalysis with the regional High-Resolution Limited-Area Model (HIRLAM). *Quarterly Journal of the Royal Meteorological Society*. **142** (698), 2119, **2016**.
9. BEZAK N., BALLABIO C., MIKOŠ M., PETAN S., BORRELLI P., PANAGOS P. Reconstruction of past rainfall erosivity and trend detection based on the REDES database and reanalysis rainfall. *Journal of Hydrology*. **590**, 125372, **2020**.
10. KIM J., HAN H., KIM B., CHEN H., LEE J. Use of a high-resolution-satellite-based precipitation product in mapping continental-scale rainfall erosivity: A case study of the United States. *Catena*. **193**, 104602, **2020**.

11. MATTHEWS F., PANAGOS P., VERSTRAETEN G. Simulating event-scale rainfall erosivity across European climatic regions. *Catena*. **213**, 106157, **2022**.
12. RAJ R., SAHARIA M., CHAKMA S., RAFIEINASAB A. Mapping rainfall erosivity over India using multiple precipitation datasets. *Catena*. **214**, 106256, **2022**.
13. DEWAN A., HU K., KAMRUZZAMAN M., UDDIN M.R. Chapter Eight - Evaluating the spatiotemporal pattern of concentration, aggressiveness and seasonality of precipitation over Bangladesh with time-series Tropical Rainfall Measuring Mission data. In: *Extreme Hydroclimatic Events and Multivariate Hazards in a Changing Environment*. MAGGIONI V. and MASSARI C., eds. Elsevier, 191, **2019**.
14. GOOVAERTS P. Using elevation to aid the geostatistical mapping of rainfall erosivity. *Catena*. **34** (3), 227, **1999**.
15. BALLABIO C., BORRELLI P., SPINONI J., MEUSBURGER K., MICHAELIDES S., BEGUERÍA S., KLIK A., PETAN S., JANEČEK M., OLSEN P., AALTO J., LAKATOS M., RYMSZEWICZ A., DUMITRESCU A., TADIĆ M.P., DIODATO N., KOSTALOVA J., ROUSSEVA S., BANASIK K., ALEWELL C., PANAGOS P. Mapping monthly rainfall erosivity in Europe. *Science of the Total Environment*. **579**, 1298, **2017**.
16. KHORSANDI N., MAHDIAN M.H., PAZIRA E., NIKKAMI D., CHAMHEIDAR H. Comparison of Different Interpolation Methods for Investigating Spatial Variability of Rainfall Erosivity Index. *Polish Journal of Environmental Studies*. **21** (6), 1659, **2012**.
17. MEUSBURGER K., STEEL A., PANAGOS P., MONTANARELLA L., ALEWELL C. Spatial and temporal variability of rainfall erosivity factor for Switzerland. *Hydrology and Earth System Sciences*. **16** (1), 167, **2012**.
18. MEDDI M., TOUMI S., ASSANI A.A. Spatial and temporal variability of the rainfall erosivity factor in Northern Algeria. *Arabian Journal of Geosciences*. **9** (4), **2016**.
19. PANAGOS P., BORRELLI P., MEUSBURGER K., YU B., KLIK A., JAE L.K., YANG J.E., NI J., MIAO C., CHATTOPADHYAY N., SADEGHI S.H., HAZBAVI Z., ZABIHI M., LARIONOV G.A., KRASNOV S.F., GOROBETS A.V., LEVI Y., ERPUL G., BIRKEL C., HOYOS N., NAIPAL V., OLIVEIRA P.T.S., BONILLA C.A., MEDDI M., NEL W., AL D.H., BONI M., DIODATO N., Van OOST K., NEARING M., BALLABIO C. Global rainfall erosivity assessment based on high-temporal resolution rainfall records. *Scientific Reports*. **7** (1), 4175, **2017**.
20. GANASRI B.P., RAMESH H. Assessment of soil erosion by RUSLE model using remote sensing and GIS - A case study of Nethravathi Basin. *Geoscience Frontiers*. **7** (6), 953, **2016v**.
21. LI X., LI Z., LIN Y. Suitability of TRMM Products with Different Temporal Resolution (3-Hourly, Daily, and Monthly) for Rainfall Erosivity Estimation. *Remote Sensing*. **12** (23), 3924, **2020**.
22. ANGULO-MARTÍNEZ M., BEGUERÍA S. Trends in rainfall erosivity in NE Spain at annual, seasonal and daily scales, 1955-2006. *Hydrology and Earth System Sciences*. **16** (10), 3551, **2012**.
23. NEARING M.A., UNKRICH C.L., GOODRICH D.C., NICHOLS M.H., KEEFER T.O. Temporal and elevation trends in rainfall erosivity on a 149 km² watershed in a semi-arid region of the American Southwest. *International Soil and Water Conservation Research*. **3** (2), 77, **2015**.
24. BECK H.E., VERGOPOLAN N., PAN M., LEVIZZANI V., van DIJK A.I.J.M., WEEDON G.P., BROCCA L., PAPPENBERGER F., HUFFMAN G J., WOOD E.F. Global-scale evaluation of 22 precipitation datasets using gauge observations and hydrological modeling. *Hydrology and Earth System Sciences*. **21** (12), 6201, **2017**.
25. RISAL A., LIM K.J., BHATTARAI R., YANG J.E., NOH H., PATHAK R., KIM J. Development of web-based WERM-S module for estimating spatially distributed rainfall erosivity index (EI30) using RADAR rainfall data. *Catena*. **161**, 37, **2018**.
26. VRIELING A., STERK G., de JONG S.M. Satellite-based estimation of rainfall erosivity for Africa. *Journal of Hydrology*. **395** (3-4), 235, **2010**.
27. CHEN Y. L., DUAN X. W., DING M. H., QI W., WEI T., LI J. D., XIE Y. New gridded dataset of rainfall erosivity (1950-2020) on the Tibetan Plateau. *Earth System Science Data*. **14** (6), 2681, **2022**.
28. QIN W., GUO Q., ZUO C., SHAN Z., MA L., SUN G. Spatial distribution and temporal trends of rainfall erosivity in mainland China for 1951-2010. *Catena*. **147**, 177, **2016**.
29. GU Z., FENG D., DUAN X., GONG K., LI Y., YUE T. Spatial and Temporal Patterns of Rainfall Erosivity in the Tibetan Plateau. *Water*. **12** (1), **2020**.
30. CAO Y., WANG S., BAI X., LI H., WANG M., WU L. Inversion calculation and spatial-temporal pattern of rainfall erosivity in southwestern China over one hundred years. *Acta Ecologica Sinica*. **38** (24), 8766, **2018**.
31. WANG Y., CHENG C., XIE Y., LIU B., YIN S., LIU Y., HAO Y. Increasing trends in rainfall-runoff erosivity in the Source Region of the Three Rivers, 1961-2012. *Science of the Total Environment*. **592** 639, **2017v**.
32. TENG H., MA Z., CHAPPELL A., SHI Z., LIANG Z., YU W. Improving Rainfall Erosivity Estimates Using Merged TRMM and Gauge Data. *Remote Sensing*. **9** (11), 1134, **2017**.
33. LIU B., TAO H., SONG C., GUO B., SHI Z., ZHANG C., BO K., HE B. Temporal and spatial variations of rainfall erosivity in China during 1960 to 2009. *Geographical Research*. **32** (2), 245, **2013v**.
34. YANG F., LU C., YUE T., YU B., LIU B. Spatiotemporal distribution of precipitation erosivity in Tibet autonomous region. *Earth System Science Data*. **14**, 665, **2022**.
35. WENBO Z., YUN X., BAOYUAN L. Spatial Distribution of Rainfall Erosivity in China. *Journal of Mountain Science*. **21** (1), 33, **2003**.
36. LIU H. Y., ZHANG G. H., ZHANG P. C., ZHU S. N. Spatial Distribution and Temporal Trends of Rainfall Erosivity in Three Gorges Reservoir Area of China. *Mathematical Problems in Engineering*. **2020** **2020**.
37. YUAN X., YANG K., LU H., HE J., SUN J., WANG Y. Characterizing the features of precipitation for the Tibetan Plateau among four gridded datasets: Detection accuracy and spatio-temporal variabilities. *Atmospheric Research*. **264**, 105875, **2021**.
38. JIANG Q., LI W., FAN Z., HE X., SUN W., CHEN S., WEN J., GAO J., WANG J. Evaluation of the ERA5 reanalysis precipitation dataset over Chinese Mainland. *Journal of Hydrology*. **595** 125660, **2021**.
39. JIAO D., XU N., YANG F., XU K. Evaluation of spatial-temporal variation performance of ERA5 precipitation data in China. *Scientific Reports*. **11** (1), 17956, **2021**.
40. MANN H.B. Nonparametric Tests Against Trend. *Econometrica*. **13** (3), 245, **1945**.

41. FORTHOFFER R.N., LEHNEN R.G. Rank Correlation Methods. In: Public Program Analysis: A New Categorical Data Approach. FORTHOFFER R.N. and LEHNEN R.G., eds. Springer US, Boston, MA, 146, **1981**.
42. WANG Z., LI J., LAI C., ZENG Z., ZHONG R., CHEN X., ZHOU X., WANG M. Does drought in China show a significant decreasing trend from 1961 to 2009? *Science of the Total Environment*. **579**, 314, **2017**.
43. YUE S., WANG C.Y. Applicability of prewhitening to eliminate the influence of serial correlation on the Mann-Kendall test. *Water Resources Research*. **38** (6), 1, **2002**.
44. TORRENCE C., COMPO G.P. A Practical Guide to Wavelet Analysis. *Bulletin of the American Meteorological Society*. **79**, 61, **1998**.
45. CHEN Y., XU M., WANG Z., CHEN W., LAI C. Reexamination of the Xie model and spatiotemporal variability in rainfall erosivity in mainland China from 1960 to 2018. *Catena*. **195**, 104837, **2020**.
46. WANG J., CHEN F., DOAN Q., XU Y. Exploring the effect of urbanization on hourly extreme rainfall over Yangtze River Delta of China. *Urban Climate*. **36**, 100781, **2021**.
47. HOVMÖLLER E. The Trough-and-Ridge diagram. *Tellus*. **1** (2), 62, **1949**.
48. WEI C., GUO B., ZANG W., YANG F., LU Y., ZHANG D., WU H., ZHEN X., XUE H., MENG C., CHEN S., YANG X., ZHANG H., HUANG X., ZHANG R. Temporal and spatial evolution patterns of drought in China over the past 500 years. *Arabian Journal of Geosciences*. **14** (9), 776, **2021**.
49. HILGARD J.E. The advance of population in the United States. *Scribner's Monthly*. **5** (4), 214, **1872**.
50. MCKEE J.J., ROSE A. N., BRIGHT E.A., HUYNH T., BHADURI B.L. Locally adaptive, spatially explicit projection of US population for 2030 and 2050. *Proceedings of the National Academy of Sciences*. **112** (5), 1344, **2015**.
51. ZHANG G., ZHANG N., LIAO W. How do population, land urbanization affect CO₂ emissions under gravity center change? A spatial econometric analysis. *Journal of Cleaner Production*. **202**, 510, **2018**.
52. KANDOGAN Y. Globalization and Shifting Economic Centers of Gravity. *Thunderbird International Business Review*. **56** (3), 261, **2014**.
53. FU X., SHEN Y., DONG R., DENG H., WU G. Analysis of urbanization based on center-of-gravity movement and characteristics in Songhua River basin of China and its southern source sub-basin between 1990 and 2010. *Chinese Geographical Science*. **26** (1), 117, **2016**.
54. XIAOLIN C., FEI Z. Gravity Center Change in the Coastal Area of the Pearl River Estuary Based on GIS and RS. In *Innovative Computing and Information. ICCIC 2011. Communications in Computer and Information Science*, Springer Berlin Heidelberg: Heidelberg, Germany, Volume 232, pp. 281, 2011.
55. LIU G., YANG Z., FATH B.D., SHI L., ULGIATI S. Time and space model of urban pollution migration: Economy-energy-environment nexus network. *Applied Energy*. **186**, 96, **2017**.
56. KRISTOUFEK L. Rescaled Range Analysis and Detrended Fluctuation Analysis: Finite Sample Properties and Confidence Intervals. *Auco Czech Economic Review*. **4** (3), 315, **2010**.
57. YUSUF H. S., MUNDAE S. V., KHAN A. R. Stock Market Data Analysis using Rescaled Range (RS) Analysis Technique. *International Journal of Engineering Research & Technology*. **3** (2), 576, **2014**.
58. SEENU P. Z., V. J. K. Comparative study of innovative trend analysis technique with Mann-Kendall tests for extreme rainfall. *Arabian Journal of Geosciences*. **14** (7), **2021**.
59. KAMAL N., PACHAURI S., HIMALAYAN U. Mann-Kendall Test - A Novel Approach for Statistical Trend Analysis. *International Journal of Computer Trends and Technology*. **63** (1), 18, **2018**.
60. SEENU P.Z., JAYAKUMAR K.V. Comparative study of innovative trend analysis technique with Mann-Kendall tests for extreme rainfall. *Arabian Journal of Geosciences*. **14** (7), 536, **2021**.
61. WANG Q., WU X., ZHAO B., QIN J., PENG T. Combined Multivariate Statistical Techniques, Water Pollution Index (WPI) and Daniel Trend Test Methods to Evaluate Temporal and Spatial Variations and Trends of Water Quality at Shanchong River in the Northwest Basin of Lake Fuxian, China. *Plos One*. **10** (4), e118590, **2015**.
62. LI W., BINGQI M. Batch Calculation of Spearman Rank Correlation Coefficient. *Environmental Protection Science*. **34** (5), 53, **2008**.
63. JUA L. Rainfall Trend Analysis of the Northwest Liaoning Province Based on Daniel and Mann-Kendall Test. *Journal of Shenyang Agricultural University*. **45** (05), 599, **2014**.
64. YI H., SHU H. The improvement of the Morlet wavelet for multi-period analysis of climate data. *Comptes Rendus Geoscience*. **344** (10), 483, **2012**.
65. YUE C., SHIJIE W., XIAOYONG B., HUIWEN L., MINGMING W., LUHUA W. Inversion calculation and spatial-temporal pattern of rainfall erosivity in southwestern China over one hundred years. *Acta Ecologica Sinica*. **38** (24), 8766, **2018**.
66. QIN W., GUO Q.K., ZUO C.Q., SHAN Z.J., MA L., SUN G. Spatial distribution and temporal trends of rainfall erosivity in mainland China for 1951-2010. *Catena*. **147**, 177, **2016**.
67. YUE T., YIN S., XIE Y., YU B., LIU B. Rainfall erosivity mapping over mainland China based on high-density hourly rainfall records. *Earth System Science Data*. **14** (2), 665, **2022**.
68. YEXI Z., YUQI L. The coupling relationship between population and economic in poyang lake ecological economic zone. *Economic Geography*. **31** (02), 195, **2011**.
69. JIE F., ANJUN T., CHEN L. The Coupling Mechanism of the Centroids of Economic Gravity and Population Gravity and Its Effect on the Regional Gap in China. *Progress in Geography*. **29** (01), 87, **2010**.
70. XU K., FANG Y., LU S. The population gravity center shift route based on environmental change in the source regions of Yangtze and Yellow Rivers --a case of Guoluo State. *Huazhong Shifan Daxue Xuebao. Ziran Kexue Ban*. **43** (4), 677, **2009**.
71. BINTAO L., HEPING T., CHUNFENG S., BING G., ZHAN S. Study on annual variation of rainfall erosivity in southwest China using gravity center model. *Transactions of the Chinese Society of Agricultural Engineering*. **28** (21), 113, **2012**.
72. THOMAS E., JOSEPH I., ABRAHAM N.P. Wavelet analysis of annual rainfall over Kerala and sunspot number. *New Astronomy*. **98**, 101944, **2023**.
73. THOMAS E., ABRAHAM N.P. Relationship between sunspot number and seasonal rainfall over Kerala using wavelet analysis. *Journal of Atmospheric and Solar-Terrestrial Physics*. **240**, 105943, **2022**.
74. PANAGOS P., BORRELLI P., MATTHEWS F., LIAKOS L., BEZAK N., DIODATO N., BALLABIO C. Global

- rainfall erosivity projections for 2050 and 2070. *Journal of Hydrology*. **610**, 127865, **2022**.
75. GUO B., ZANG W.Q., YANG F., HAN B.M., CHEN S.T., LIU Y., YANG X., HE T.L., CHEN X., LIU C.T., GONG R. Spatial and temporal change patterns of net primary productivity and its response to climate change in the Qinghai-Tibet Plateau of China from 2000 to 2015. *Journal of Arid Land*. **12** (1), 1, **2020**.
76. BINTAO L., HEPING T., CHUNFENG S., BING G., ZHAN S., CHAO Z., BO K., BING H. Temporal and spatial variations of rainfall erosivity in China during 1960 to 2009. *Geographical Research*. **32** (02), 245, **2013**.
77. KEYUAN Z., FENLI Z. Spatial and Temporal Variation Characteristics of Rainfall Erosivity in the Songhua River Basin from 1960 to 2014. *Journal of Natural Resources*. **32** (02), 278, **2017**.
78. LIU S., HUANG S., XIE Y., LENG G., HUANG Q., WANG L., XUE Q. Spatial-temporal changes of rainfall erosivity in the loess plateau, China: Changing patterns, causes and implications. *Catena*. **166**, 279, **2018**.
79. JIA L., YU K., LI Z., LI P., ZHANG J., WANG A., MA L., XU G., ZHANG X. Temporal and spatial variation of rainfall erosivity in the Loess Plateau of China and its impact on sediment load. *Catena*. **210**, 105931, **2022**.
80. XU X., YAN Y., DAI Q., YI X., HU Z., CEN L. Spatial and temporal dynamics of rainfall erosivity in the karst region of southwest China: Interannual and seasonal changes. *Catena*. **221**, 106763, **2023**.
81. TU A., ZENG J., LIU Z., ZHENG H., XIE S. Effect of minimum inter-event time for rainfall event separation on rainfall properties and rainfall erosivity in a humid area of southern China. *Geoderma*. **431**, 116332, **2023**.